Chemical Engineering Journal 453 (2023) 139791

Contents lists available at ScienceDirect

Chemical Engineering Journal

journal homepage: www.elsevier.com/locate/cej

Thermochemical syngas generation via solid looping process: An experimental demonstration using Fe-based material

Christopher de Leeuwe [a], Syed Zaheer Abbas [a], Panagiotis Alexandros Argyris [a], Adam Zaidi [a], Alvaro Amiero [b], Stephen Poultson [b], David Wails [b], Vincenzo Spallina [a,*]

[a] Department of Chemical Engineering and Analytical Science, University of Manchester, Manchester M13 9PL, United Kingdom
[b] Johnson Matthey Technology Centre, Reading RG4 9NH, United Kingdom

ARTICLE INFO

Keywords:
Chemical looping
CO_2 capture
H_2 production
Packed bed reactor
High pressure

ABSTRACT

Chemical looping is investigated for the production of syngas via reforming or reverse water gas shift in a packed bed reactor using 500 g of Fe on Al_2O_3 was demonstrated. Oxidation, reduction of the OC and subsequent catalytic reactions of reforming or reverse water gas shift were examined in a temperature range of 600–900 °C and a pressure range of 1–3 bar_a at high flowrate. Different inlet gas compositions were explored for the considered gas–solid and catalytic reaction stages. Oxidation with air successfully heated the reactor. CH_4 resulted ineffective at reducing the Fe-based oxygen carrier while H_2 and CO-rich stream were able to achieve full reduction to FeO of the material. In terms of catalytic activity, the maximum conversion of CH_4 achieved during the reforming was limited to 62.8 % at 900 °C and 1 bar_a.

Thermally integrated chemical looping reverse water gas shift was studied as option for CCU in combination with green H_2 to produce renewable fuels. A H_2/CO value of 2 could be achieved by feeding H_2/CO_2 of 2. The pressure did not substantially affect the conversion and the bed did not present carbon deposition.

The ability of a Fe-based packed bed chemical looping reactor to recover after the carbon deposition was also explored. It was found that using a mixture of CH_4 and CO_2 achieved 92% recovery of the original capacity.

1. Introduction

Hydrogen and gas-to-liquid (GTL) processes for ammonia, methanol or Fischer-Tropsch fuels are of vital importance in the global chemical products market. A significant fraction (60 %) of the global demand for these products is satisfied by the reforming of natural gas (NG), oil and naphtha [1]. A large fraction of the chemical industry's CO_2 emissions are produced by the conventional methods and systems that are used to carry out steam methane reforming [2]. These conventional techniques also come at high operational and capital costs.

Two methods for reforming dominate the industrial strategies. These are fired tubular reforming (FTR) or auto thermal reforming (ATR). The key difference between these processes is how the heat to drive the endothermic reforming reaction is provided. In the FTR reactor, the NG and either H_2O or CO_2 (Eqs. (1) or (2)) are co-fed through the tubes filled with the catalyst while the outside of the tubes is immersed in a furnace where fuel is burnt with air. The combustion provides the necessary heat for the reforming reaction. In contrast, in the ATR, air or oxygen is added to allow the exothermic CH_4 partial oxidation (Eq. (3)) [3] so that the reaction does not need an additional external heat source although high electricity consumption occurs for air compression or oxygen separation. Both these methodologies require actions to reduce greenhouse emissions. This can be carried out via solvent absorption or through the use of membrane systems which result in high costs per ton of CO_2 avoidance (the avoidance cost of CO_2 is between 47 and 70 €/t depending on the capture rate and technology used) [4,5].

$$CH_4 + H_2O \leftrightarrow 3H_2 + CO \qquad \Delta H^0_{298K} = 206 \frac{kJ}{mol_{CH_4}} \tag{1}$$

$$CH_4 + CO_2 \leftrightarrow 2H_2 + 2CO \qquad \Delta H^0_{298K} = 247 \frac{kJ}{mol_{CH_4}} \tag{2}$$

$$CH_4 + 0.5O_2 \leftrightarrow 2H_2 + CO \qquad \Delta H^0_{298K} = -36 \frac{kJ}{mol_{CH_4}} \tag{3}$$

In the long term, the increasing production of green H_2 via water electrolysis and the availability of large amounts of CO_2 at high purity from industrial processes (e.g. steel, cement, refinery), bio-energy CCS

* Corresponding author.
E-mail address: vincenzo.spallina@manchester.ac.uk (V. Spallina).

https://doi.org/10.1016/j.cej.2022.139791
Received 13 July 2022; Received in revised form 4 October 2022; Accepted 11 October 2022
Available online 15 October 2022

Nomenclature

Abbreviations

AR	Air reactor
ATR	Autothermal reforming
CLC	Chemical looping combustion
CLR	Chemical looping reforming
CLR-PB	Chemical looping reforming in packed bed reactors
DMR	Dry methane reforming
FR	Fuel reactor
FTR	Fired Tubular Reforming
GTL	Gas to liquid
NLPM	Normal liter per minute
OC	Oxygen carrier
RWGS	Reverse water gas shift
SMR	Steam methane reforming
TEM	Transmission electron microscopy
TC	Thermocouple
TRL	Technology readiness levels
WGS	Water gas shift
XRD	X-ray diffraction

Symbols

$c_{p,g}$	gas specific heat capacity, J kg^{-1} K^{-1}
$c_{p,s}$	solid specific heat capacity, J kg^{-1} K^{-1}
$\Delta H_{R,ox}$	enthalpy of reaction for oxidation, J/mol
MW_{O_2}	O_2 molecular weight, kg mol^{-1}
$MW_{OC,act}$	Active OC molecular weight, kg mol^{-1}
T	Temperature, °C
u_s	Superficial gas velocity, m_g^3 m_r^{-2} s^{-1}
ξ	O_2 to solid mole oxidation reaction ratio
$\omega_{gO_2,0}$	Initial O_2 mass fraction
$\omega_{OC,act}$	Active OC solid mass fraction

(BECCS) or direct air capture (DAC) could be a solution to improve sustainability and reduce the reliance of fossil fuels. Green hydrogen and recycled CO_2 are mostly studied to produce CO-rich syngas by the reverse water gas shift (RWGS) reaction (Eq. (4)) [6]. Due to the thermodynamic limitations, RWGS is endothermic and requires high temperatures (>800 °C) to achieve a suitable CO yield. This could be achieved through either a high electrical load [7] or through chemical heat.

$$CO_2 + H_2 \leftrightarrow H_2O + CO \qquad \Delta H^0_{298K} = 41 \frac{kJ}{mol_{H_2}} \tag{4}$$

Chemical looping has demonstrated to be an effective technology for the inherent separation of gaseous products by uncoupling the fuel combustion and avoiding the CO_2 dilution with N_2 from air [8]. Compared to oxygen-blown technologies do not require an air separation unit to produce pure oxygen. The heat generated during chemical looping combustion is transferred to an endothermic reaction without indirect heat transfer equipment operated at high temperatures. Moreover, the separation of product gas into syngas, oxygen-depleted air and CO_2-rich stream make this technology suitable for CCUS with reduced cost of CO_2 avoidance. By inherently lowering the cost of carbon capture this can improve plant profitability under green incentives or carbon taxes [9].

The separation is achieved through the use of a solid metal oxide also called oxygen carrier (OC) [10]. The metal oxide oxidation (Eq. (5)) and reduction (Eq. (6)) result in a generation of heat which can be used for steam methane reforming (SMR) where H_2O is utilized or dry methane reforming (DMR) which uses CO_2 instead (Eqs. (1) and (2)) or RWGS (Eq. (4)).

$$2Fe_3O_4 + 0.5O_2 \leftrightarrow 3Fe_2O_3 \qquad \Delta H^0_{298K} = -472 \frac{kJ}{mol_{O_2}} \tag{5}$$

$$9Fe_2O_3 + CH_4 \leftrightarrow 6Fe_3O_4 + CO + 2H_2O \qquad \Delta H^0_{298K} = 141 \frac{kJ}{mol_{CH_4}} \tag{6}$$

In this paper, the use of chemical looping to supply heat to generate syngas via RWGS is also presented as an alternative, long-term route (CLRWGS as for the reaction in Eq. (4)).

Most literature work has focused on chemical looping fluidised bed systems [5,11–13] which work at atmospheric pressure. However, high pressure is preferable for industrial processes for both CO_2 removal and uses of syngas in downstream processes (methanol, ammonia, liquid fuel synthesis), thus dynamically operated packed bed reactors have been proposed (Fig. 1) [14].

Chemical looping in dynamically operated packed bed reactors have been demonstrated using Ni, Fe, Cu and Mn-based OCs up to early TRL5 to generate the heat required for CO_2-free electricity [15] and the process has been comprehensively assessed from a techno-economic point of view [16].

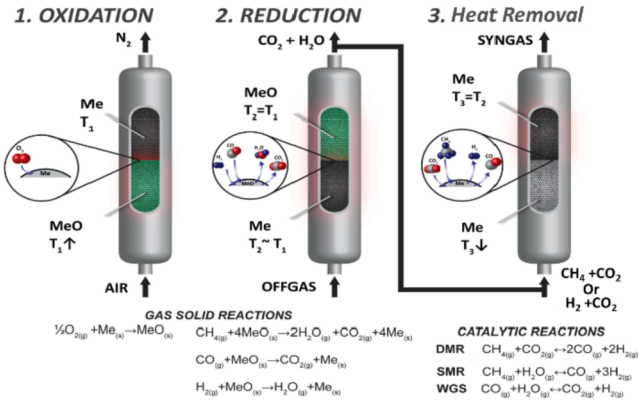

Fig. 1. Schematic of CLR or CLRWGS process steps.

In terms of the OC, Fe-based materials are expected to be cheaper compared to Ni-based materials but they have slow kinetics. The reduction is limited to FeO as the formation of pure Fe increases sintering and carbon deposition [17]. However, Fe-based catalysts are widely used to promote high-temperature WGS reaction [18] which makes the combination of chemical looping and RWGS an appealing alternative.

The exact composition of the OC is of vital importance as sufficient Fe-based material must be present to catalyse the RWGS reaction and provide the heat to drive the reaction. However, too much Fe-based OC could result in unacceptable hot spots during oxidation. This means that the active weight content on the support material must be limited. In the latter case, cycle time is shorter than previously studied with chemical looping reforming. The increased temperature improves oxidation kinetics. In these conditions, the RWGS kinetics at these temperatures (600–900 °C) are favourable without catalyst [19] and improved further in the presence of Fe and FeO [18,20,21] so this allows for the heat generation requirements to dominate, leaving a larger degree of freedom in the design of the OC.

This work will present the performance of Fe-based OC in a packed bed reactor comparing the effect of pressure, temperature, H_2, CO_2, CO,

and CH_4 in a large lab-scale setting under relevant industrial conditions. Also, the OC regeneration after carbon deposition was assessed using different methods to determine the effect on the OC capacity of the material, including air treatment, CO_2 treatment and use of reforming mixtures.

2. Methodology

2.1. Experimental setup

A simplified schematic of the packed bed reactor rig used in this study is shown in Fig. 2. The setup consists of a high-temperature resistant stainless-steel tube (253MA) with an inner diameter of 35 mm and a length of 1050 mm (manufactured by Array Industries BV). A 6.3 mm ID multiple point thermocouple, with 10 measurement points every 75 mm is used to obtain the unsteady axial temperature profile, this multipoint thermocouple measurement allows for measurement to be taken every second to a precision of 0.01 °C. The reactor is heated using a jacketed Carbolite furnace. To mitigate the heat losses, the pipework before and after the reactor was insulated using ceramic wool. The composition and feed flowrate are controlled by Bronkhorst mass flow controllers and pressure is controlled by a back-pressure regulator sensor (Bronkhorst). The reactor exhaust is cooled to remove any water content before the dry gas composition is determined using a combination of a mass spectrometer (Hiden QGA) coupled with a CO analyser (Siemens). The mass spectrometer is capable of high precision measurement (0.1 % of the molar gas fraction). The complete methodology used for gas phase calculations was detailed in the SI of de Leeuwe et al. [22].

The reactor was filled with inert material (Al_2O_3) [23] at the bottom and top to ensure that the OC material is held in the middle of the reactor where the temperatures are most tightly controlled. This also allowed for some preheating of the inlet gas to the reaction temperature. The middle of the reactor was packed with 500 g of a Fe-based OC supported on Al_2O_3. The batch of Fe-based material was prepared by wet impregnated using a Fe precursor on Al_2O_3 spheres by Johnson Matthey. The Particle size was ranging from 1000 to 1500 μm. The total length of the reactive material inside the bed was 400 mm. This packed bed covered the thermocouples TC4 to TC8, with thermocouple TC3 located just before the start of the reactive section as shown in Fig. 2.

3. Results and discussion

3.1. Oxidation stage

The experimental conditions tested for the oxidation are recorded in Table 1. He was used as a tracer gas so that the length of the oxidation could be measured, 10.5 % O_2 was used as the base case to limit the exothermic nature of the oxidation. The bed is reduced consistently to the same conditions prior to each oxidation using 10 NLPM flowrate, 1 bar_a at 800 °C with a composition of 10 % H_2, 40 % CO_2 until the outlet gas composition became steady, any variation in gas composition or temperature over 10 min being less than the uncertainty in its measurement. Under these conditions, OC is available as FeO [24]. This fact along with a consistent temperature profile at the end of each reduction means that for each oxidation the bed composition is consistent so comparisons between oxidation conditions will not be affected by a changing bed composition.

Table 1
Experimental conditions used for the oxidation stage.

Reactor set point (°C)	Flowrate (NLPM)	Pressure (bar_a)	Feed gas (% molar)
400	10	1 and 3	O_2 10.5 % He 10 % in balance of N_2
500	10	1 and 3	O_2 10.5 % He 10 % in balance of N_2
600	10	1 and 3	O_2 5.25 %, 10.5 % or 19.5 %, He 10 % in balance of N_2
700	10	1 and 3	O_2 5.25 %, 10.5 % and 19.5 %, He 10 % in balance of N_2

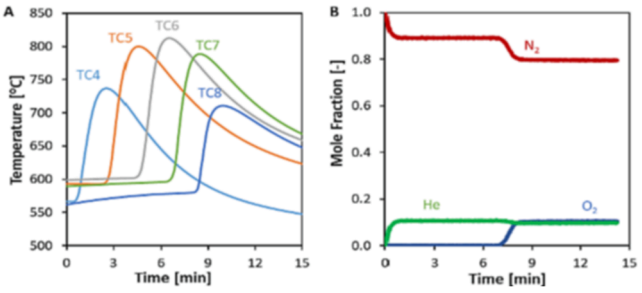

Fig. 3. Dynamic temperature profile (A) and outlet gas composition (B) during the oxidation at 1 bara, 10 NLPM feed flowrate, 600 °C initial bed temperature and 10.5 % O_2 in the feed.

The oxidation of FeO to Fe_2O_3 is exothermic ($\Delta H^0 = -560$ kJ/mol_{O2}), causing the reaction to move through the bed and heating it progressively. After the reaction front has passed, that section of the bed cools due to forced convection and the heat losses associated with a small laboratory rig. In Fig. 3a, it is possible to see that TC4 is located at the beginning of the bed (z = 0 mm) and it experiences a small temperature rise due to the initial lower temperature and high heat losses associated with the more external zone of the bed. TC8 does not experience the same rise compared to the central three thermocouples as it is almost out of the bed and in contact with the inert support. This sharp front seen in the temperature profile data is reflected also in the outlet gas composition (Fig. 3b) where the O_2 breakthrough is recorded after the first 7 min and it takes about 30 s to achieve the inlet composition. The recorded temperature never exceeded 1000 °C so the chances of material degradation are reduced, meaning that the Fe content of the material is in an acceptable range from a heat generation point.

3.1.1. Effect of initial solid temperature

The effect of the initial solid temperature on the temperature profile and gas conversion was measured under the operating conditions of 10 NLPM feed flowrate, 1 bar_a and 10.5 % O_2 in the feed. The results are illustrated in Fig. 4. This shows that at higher initial solid temperature the time for the O_2 breakthrough increases, indicating a larger OC (and reactivity). The O_2 capacity at 400 °C (0.336 ± 0.002 mol oxygen per kg of OC) is considerably lower than that of the other temperatures (500–700 °C) not fitting the same pattern, therefore not suitable to drive

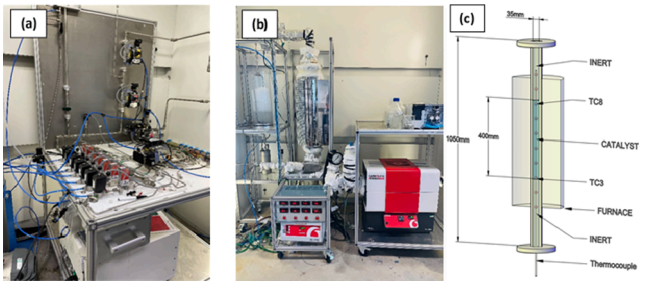

Fig. 2. Lab scale packed bed reactor set-up located at the University of Manchester having (a) an inlet dry gas feeding system in FC-1; (b) a packed-bed reactor enclosed in a furnace placed in FC-2 and (c) schematic diagram of the packed-bed reactor unit.

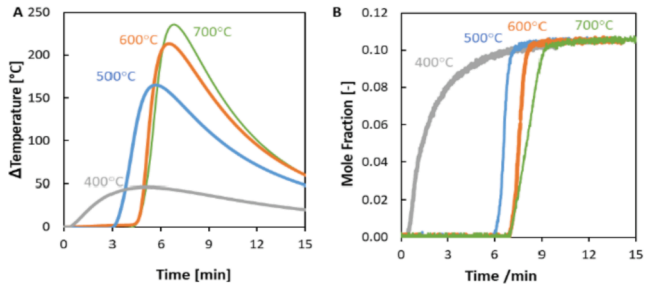

Fig. 4. The change in temperature at TC6 (z = 0.225 m) (A) and outlet O_2 mole fraction (B) as a function of time at various temperatures for 10.5 % O_2, 10 NLPM and 1 bar_a.

the reaction, explaining why breakthrough is almost immediate and reaching steady state takes considerably longer than the other temperatures. This is also confirmed by the much lower temperature rise exhibited at 400 °C (compared to higher initial solid temperature). At 500 °C the breakthrough occurs much later giving an oxygen capacity of 1.068 ± 0.002 mol oxygen per kg of OC, however, the effect of the initial temperature is still notable with early breakthrough and lower oxygen capacity than the higher temperatures. The increased temperature improves oxidation kinetics, which allows for more the material to react as accounted for with a shrinking core model of the OC, when the temperature increases the shell of the material that can react is greater.

In case of T > 600 °C, the O_2 breakthrough occurs at 7 min for both tested temperatures but they have slightly different oxygen capacities; 1.238 ± 0.002 mol oxygen per kg of OC at 600 °C and 1.346 ± 0.002 mol oxygen per kg of OC at 700 °C. This difference is only in the time to reach a steady composition due to a smaller increase in the oxygen carrier capacity. The same results are observed in terms of temperature rise, where the maximum ΔT is recorded at the initial solid temperature of 700 °C (+229 °C). This temperature rise corresponds to a weight Fe_2O_3 content in the OC of 24 % (weight fraction) according to Eq. (7), however, this Fe_2O_3 content may be higher as the temperature rise in the material is 100–150 °C higher than the one recorded from the thermocouple as recently demonstrated in Argyris et al.[25].

$$\Delta T_{MAX} = \frac{\left(-\Delta H_{R,ox}\right)}{\frac{c_{p,s}MW_{OC,act}}{\omega_{OC,act}\xi} - \frac{c_{p,g}MW_{O_2}}{\omega_{gO_2,0}}} \tag{7}$$

3.1.2. Effect of reactor pressure

Oxidation tests were carried out at 700 °C using 10.5 % O_2 in a total flow of 10 NLPM at 1 and 3 bar_a conditions. The effect on the temperature rise in the reactor and the nature of the breakthrough of O_2 at the reactor outlet are compared in Fig. 5. Only TC6 is plotted as it underwent the highest temperature change. It was found that pressure did not have a measurable effect on the O_2 breakthrough time but did slightly alter the shape of the response, with the 3 bar_a response rising quicker, but this effect is very slight. While the breakthrough times for both materials are very similar, there is a slight difference in the effective oxygen content of the material at these different pressures, 1.378 ± 0.002 mol oxygen per kg of OC for 3 bar and 1.346 ± 0.002 mol oxygen per kg of OC for 1 bar. This small effect of pressure s is a deviation from the response seen in Argyris et al. [26] who showed a measurable effect of the pressure. The lack of effect using this Fe-based material could be due to this material being wet impregnated for these experiments and this means that most of the Fe ions present in the material are clustered near the surface so the increased pressure forces the gas deeper into the cracks on the material does not increase the capacity of the bed as much as was the case for OCs produced using other methods. This effect has been previously seen in Cu-based OC prepared via this method [27]. However further tests at different pressure are required to extrapolate a defined pattern.

3.1.3. Effect of oxygen concentration

In this section, the effect of O_2 concentration on the breakthrough and the change in temperature of the reactor is examined at 1 bar_a, 10 NLPM and starting solid temperature of 600 °C. Fig. 6 shows that breakthrough time increases with each decrease in O_2 concentration. Additionally, the shape of the breakthrough curve changes, with the high giving increased the oxidations kinetics confirming the results obtained also for Ni-based OC [26,28]. The changing O_2 concentrations in the gas feed also affect the oxygen capacity of the material, with the highest O_2 concentration having the lowest capacity, 1.230 ± 0.002 mol oxygen per kg of OC, and a steady increase in capacity as the concentration drops, 1.238 ± 0.002 mol oxygen per kg of OC and 1.384 ± 0.002 mol oxygen per kg of OC respectively. This can also be seen in the breakthrough times with the ratio between initial breakthrough time being slightly less than the reciprocal of the concentrations. The lowest mole fraction of oxygen gives the largest oxygen capacity because the prolonged oxidation time allows for the OC material at the entrance and exit of the bed that are at lower temperatures more time to slowly react increasing the capacity of the bed slightly. [29,30].

3.2. Reduction stage

The experimental conditions tested for the reduction of the Fe-based material are recorded in Table 2. Before each reduction, oxidation was carried out under the same conditions using 10 NLPM flowrate, 1 bar_a at 600 °C with a composition of 5.25 % O_2, 10 % He in a balance of N_2 until the outlet gas composition became steady, any variation in gas composition over 10 min being less than the uncertainty in its measurement. This results in the OC being fully oxidised to Fe_2O_3 [24].

The reduction stage used a mixture of H_2 and CO_2. This mixture was used to ensure that metallic Fe was not formed during the reduction in the range of temperatures considered according to the thermodynamic equilibrium. Due to the presence of H_2 and CO_2, the catalytic RWGS reaction takes place and the outlet composition of the gas products is different from the inlet composition after the breakthrough has occurred

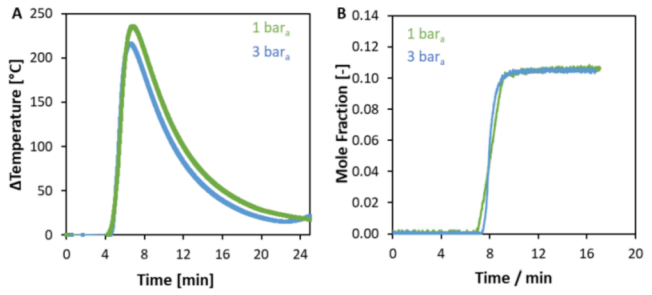

Fig. 5. The change in temperature at TC6 (z = 0.225 m) (A) and outlet O_2 mole fraction (B) as a function of time at 1 and 3 bar_a for 10.5 % O_2, 10 NLPM and 700 °C.

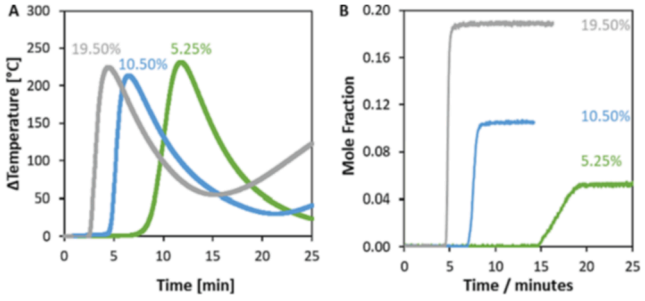

Fig. 6. The change in temperature at TC6 (z = 0.225 m)) (A) and outlet O_2 mole fraction (B) as a function of time at various oxygen feed mole fractions, 1 bara, 10 NLPM and 600 °C.

Table 2
Experimental conditions used for the reduction of Fe-based OC.

Reactor set point (°C)	Flowrate (NLPM)	Pressure (bar_a)	Gas composition (molar %) with balance in He
600	10	1 and 3	10 % H_2 40 % CO_2 10 % H_2 10 % CO 70 % CO_2
700	10	1 and 3	10 % H_2 40 % CO_2 10 % H_2 10 % CO 70 % CO_2 10 % CH_4 70 %CO_2 (1 bar_a only)
800	10	1 and 3	10 % H_2 40 % CO_2 10 % H_2 10 % CO 70 % CO_2
850	10	1 and 3	10 % H_2 40 % CO_2 10 % H_2 10 % CO 70 % CO_2

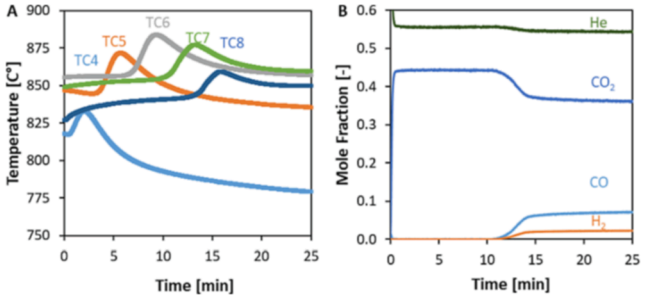

Fig. 7. Recorded temperature (A) and outlet gas composition (B) during reduction at 1 bar_a, 10 NLPM feed flowrate, 850 °C initial bed temperature and 10 % H_2 and 40 % CO_2 in the feed.

and the bed is fully reduced (Fig. 7b).

The reduction with H_2 from Fe_2O_3 to FeO is slightly exothermic ($\Delta H = -10$ kJ/mol_{FeO}; T = 800 °C [31]), with an increase in temperature moving along the bed, thus causing a smaller change in temperature at each point in the bed. Once the bed is reduced, the temperature starts to drop but the beginning of the bed drops below its initial starting condition and below the set point of the furnace due to the RWGS reaction. The breakthrough starts after 11 min, and it takes 4 min to show a stable profile demonstrating the good reactivity of the material in presence of H_2/CO_2 mixture.

3.2.1. *Effect of initial solid temperature*

The effect of the initial solid temperature on the reduction was also explored and the results can be seen in Fig. 8. By increasing the initial solid temperature, it is possible to notice that:

- The maximum temperature rise detected by TC6 decreases due to a higher extent of the RWGS conversion, which is favoured at higher temperatures.

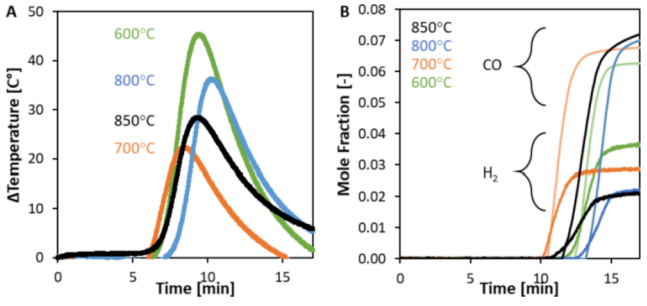

Fig. 8. The change in temperature at TC6 (z = 0.225 m) (A) and outlet H_2 (and CO) mole fraction (B) as a function of time at various temperatures during reduction for 10 % H_2, 10 NLPM and 1 bara.

- It is not possible to identify a linear trend in the H_2 breakthrough since it appears at the reactor outlet due to the combination of an increase of the bed capacity (at higher temperature the more Fe_2O_3 is converted during the reduction), but also because the conversion of $H_2 + CO_2$ into CO reduces the Fe_2O_3 conversion with fuel since the reaction rate of Fe_2O_3 reduction with H_2 is much faster than with CO [32,33].
- The final solid composition may change thus forming a different ratio of FeO/Fe_3O_4/Fe, including hercynite [34] therefore the slope of H_2/CO breakthrough does vary but not following a trend.

3.2.2. *Effect of reactor pressure*

Fig. 9 shows the effect of pressure on the outlet molar composition of the H_2 and rise in temperature at TC6 (z = 0.225 m) during the reduction stage under the operating conditions of 10 % H_2 40 % CO_2 at 850 °C and 10 NLPM total flowrate. At 3 bar_a, the breakthrough occurs with 2 min delay than the case at 1 bar_a and a later rise in temperature, potentially showing that more material is reduced at higher pressure. The increased pressure did not have a large effect on the change in temperature during reduction, with only a 1 °C difference between the peaks. The pressure did affect the extent of the RWGS on the outlet gas composition with the

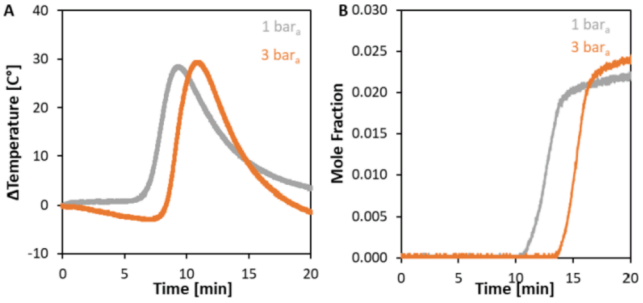

Fig. 9. The change in temperature at TC6 (z = 0.225 m) (A) and outlet H_2 mole fraction (B) as a function of time at 1 and 3 bar during reduction for 10 % H_2 and 40 % CO_2, 10 NLPM and 850 °C.

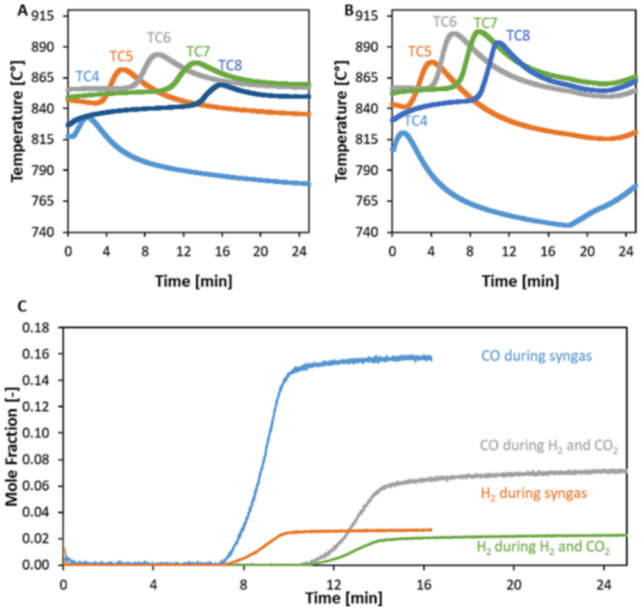

Fig. 10. Comparison between recorded temperature (A and B) and outlet gas composition (C) during reduction at 1 bara with either 10 % H_2 and 40 % CO_2 (A) or10% H_2, 10 %CO and 70 % CO_2 (B) in the feed. The controlled conditions were set at 10 NLPM feed flowrate, 850 °C initial bed temperature and 1 bara.

increased pressure having a slightly larger H_2 proportion (2.35 % H_2 in the outlet versus 2.14 % H_2), this is also seen at lower temperatures as detailed in SI Fig. 1-S.

3.2.3. Reduction using syngas

The outlet gas composition and temperature profile during reduction at 850 °C, 1 bar_a and 10 NLPM using respectively 10 % H_2 and 40 % CO_2 and syngas representative of a PSA off gas (10 % H_2, 10 %CO and 70 % CO_2) are compared in Fig. 10. In presence of CO, the higher amount of reactive gas results in a faster breakthrough and earlier temperature peaks.

The larger ratio of reducing agents to CO_2 is also seen in the outlet gas composition where the CO and H_2 content is varied accordingly thus exhibiting an increase of CO and reduction of H_2.

The effect of initial solid temperature on the temperature rises and the H_2 breakthrough represented in Fig. 11 shows that at a temperature above 600 °C, the solid conversion increases significantly. This provides clear information at the design level where reduction should be carried out at higher temperature, especially in presence of CO. It can also be seen that once the bed temperature reaches 850 °C the breakthrough occurs earlier than at 800 °C but a consistent drop in mole fraction is seen, this is most likely due to the diminishing improvements in the kinetics being overcome by faster gas velocity that occurs at high temperatures.

The effect of pressure is marginal as reported in Fig. 12 shows thus with a limited impact in the conversion and a slightly delayed breakthrough.

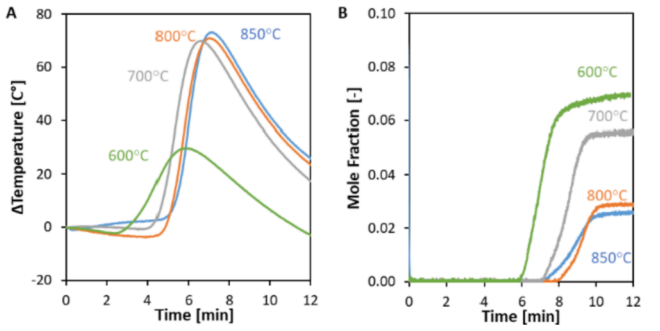

Fig. 11. The change in temperature at TC6 (z = 0.225 m) (A) and outlet H_2 mole fraction (B) as a function of time at various temperatures during reduction for a mixture of 10 % H_2 and 10 % CO, 10 NLPM and 1 bar_a.

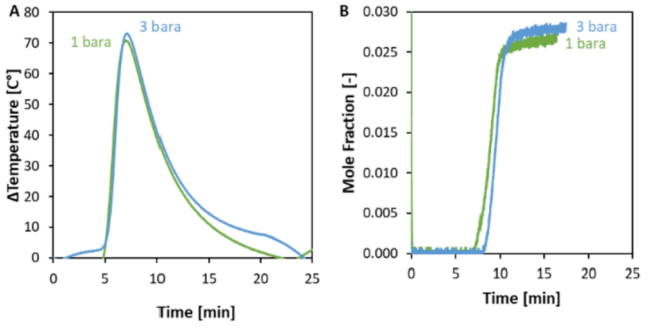

Fig. 12. The change in temperature at TC6 (z = 0.225 m) (A) and outlet H_2 mole fraction (B) as a function of time at 1 and 3 bar_a during reduction for a mixture of 10 % H_2 and 10 % CO, 10 NLPM and 850 °C.

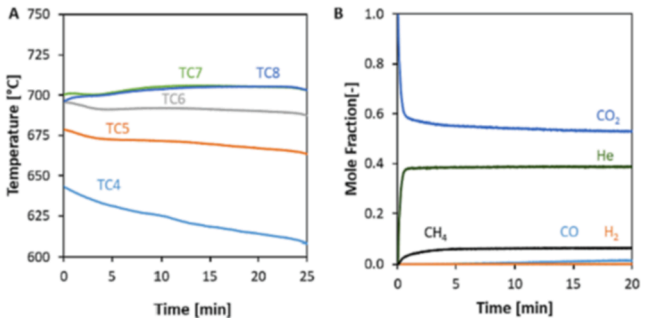

Fig. 13. Recorded temperature (A) and outlet gas composition (B) during reduction at 1 bar_a, 10 NLPM feed flowrate, 850 °C initial bed temperature and 10 % CH_4 and 70 % CO_2 in the feed.

3.2.4. Reduction with CH_4-based fuel

The response to reduction using 20 % synthetic biogas (assuming 50 % CH_4 and 50 % CO_2) diluted with CO_2 (60 % CO_2) with the remainder inert gases are shown in Fig. 13 to highlight the effect of CH_4 fuel in the reduction of Fe_2O_3. The CH_4-based gas mixture was not effective at reducing the packed bed. The CH_4 conversion was very low, only 15 % of the CH_4 fed reacted with the Fe_2O_3. This can also be seen in the temperature profile where most of the bed does not change in temperature during the 20 min reduction. A small temperature decrease is recorded in TC3 and TC4 at the beginning of the bed where part of the CH_4 is reducing Fe_2O_3 to FeO ($\Delta H^0_{298K} = 318.4 \frac{kJ}{mol_{CH_4}}$). This demonstrates that CH_4-based feedstock is not effective unless Fe is mixed/doped with Ni forming a bi-metallic OC [35,36].

3.3. Dry reforming

The reforming gas conditions and compositions tested are listed in Table 3. Based on the thermodynamic limitations of such a system CO_2 to CH_4 ratios of 5, 6 and 7 were selected to maximise CH_4 conversion and avoid carbon deposition [37].

The temperature profile and outlet gas composition during dry reforming of CH_4 at 1 bar_a, 12 NLPM feed flowrate, 900 °C initial bed temperature and 8.3 % CH_4 and 50 % CO_2 can be seen in Fig. 14. Additionally, the conversion of CH_4 in the reactor is also plotted alongside the outlet gas composition. The Fe-based OC achieved only a 58.7 % conversion on average during the reforming. The low reforming activity can be seen in the temperature data which show that the temperature in the reactor drops by 68 °C compared to 148 °C in the case of Ni-based catalyst [26]. After 12 min, the power to the furnace was stopped to see the effect of dropping temperature and the results show an increase in the selectivity towards H_2 and CO_2 in the products along with a drop in the CH_4 conversion (Fig. 14). Compared to the reduction with the CH_4-based mixture previously examined, the presence of FeO favours the CH_4 conversion while in case of Fe_2O_3, CH_4 breakthrough was almost immediate (Fig. 14).

Table 3
Reforming experimental conditions.

Reactor set point (°C)	Flowrate (NLPM)	Pressure (bar_a)	Gas composition (molar %) with balance in He
700	12	1, 3 and 5	8.3 % CH_4 58.3 %CO_2
			8.3 % CH_4 50.0 %CO_2
			8.3 % CH_4 41.7 %CO_2
800	12	1 and 3	8.3 % CH_4 58.3 %CO_2
			8.3 % CH_4 50.0 %CO_2
			8.3 % CH_4 41.7 %CO_2
850	12	1 and 3	8.3 % CH_4 60 %CO_2
900	12	1 and 3	8.3 % CH_4 58.3 %CO_2
			8.3 % CH_4 50.0 %CO_2
			8.3 % CH_4 41.7 %CO_2

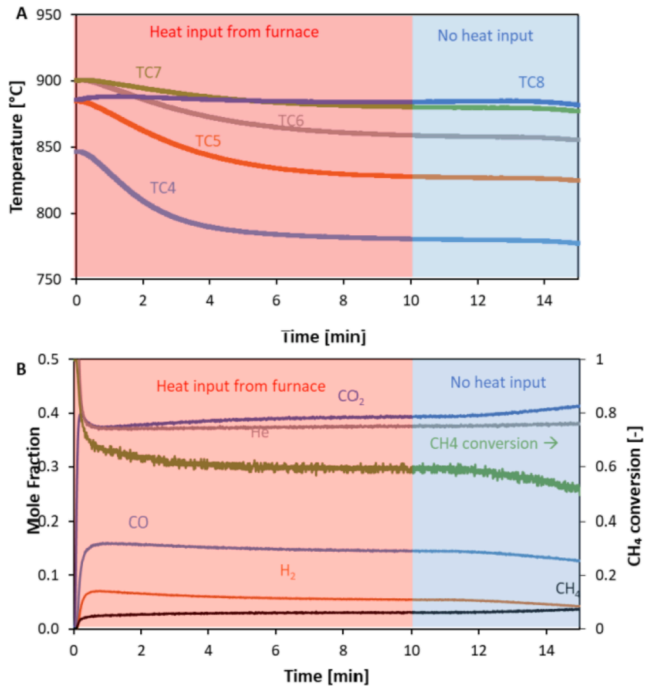

Fig. 14. Recorded temperature (A), outlet gas composition and CH_4 conversion (B) during reforming at 1 bar_a, 12 NLPM feed flowrate, 900 °C initial bed temperature and 8.3 % CH_4 and 50 % CO_2 in the feed.

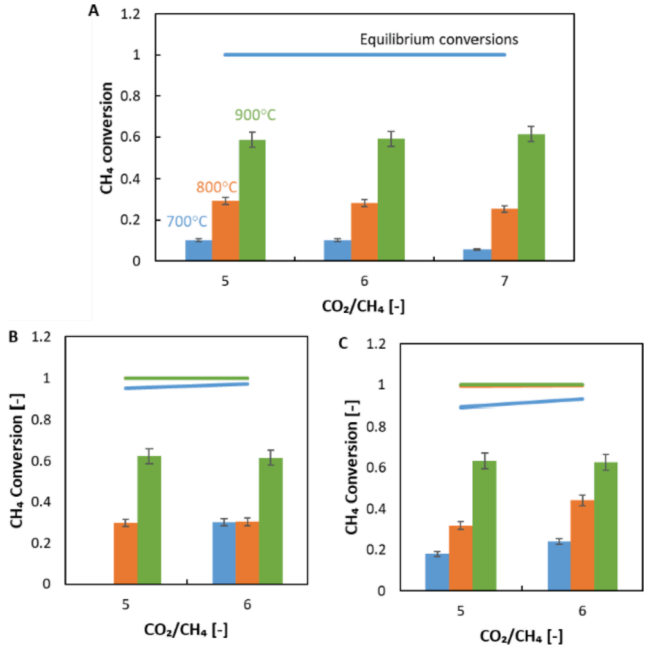

Fig. 15. CH_4 conversion at 1 bar_a (A), 3 bar_a (B) and 5 bar_a (C) as a function of temperature and CH_4:CO_2 ratio at a total flowrate of 12 NLPM as measured experimentally (bar) compared with equilibrium conditions (lines).

The effect of temperature, pressure and CO_2-to-CH_4 ratio on CH_4 conversion is presented in Fig. 15. At 1 bar and with a molar CO_2/CH_4 ratio of 5 increasing temperatures from 700 to 900 °C increases the CH_4 conversion from 10.2 to 58.7 %. A similar effect is seen at different CO_2 to CH_4 ratios. The increase of the temperature improves the kinetics of the reaction along with a more favourable equilibrium. The more favourable kinetics also prevails in the conversion compared to the thermodynamic effect (Fig. 15A vs Fig. 15B vs Fig. 15C).

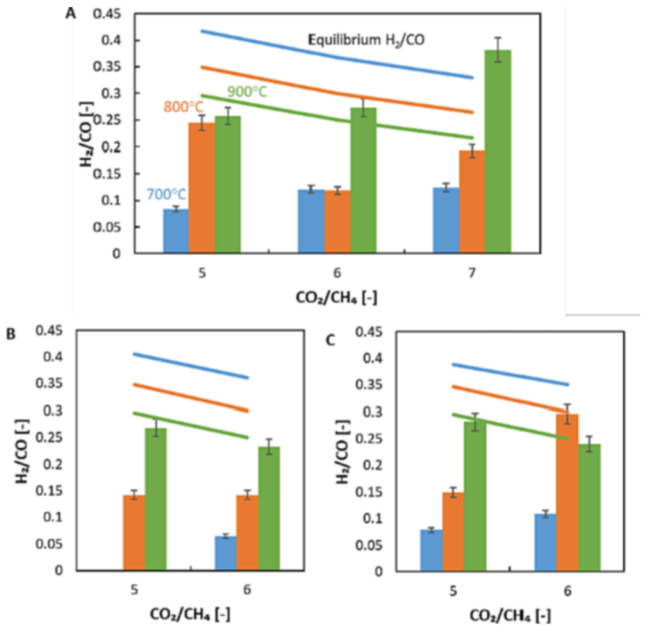

Fig. 16. H_2/CO ratio at 1 bar_a (A), 3 bar_a (B) and 5 bar_a (C) as a function of temperature and CH_4:CO_2 ratio at a total flowrate of 12 NLPM as measured experimentally (bar) compared with equilibrium conditions (lines).

In terms of syngas composition, the outlet H_2/CO ratio is shown in Fig. 16. The results here are dominated by the conversion (kinetics) of the CH_4, thus the H_2/CO ratio that increases when CH_4 conversion also increases. The same effect is also detected at higher CH_4-to-CO_2 ratio.

It can be seen in Fig. 16A that when the CO_2/CH_4 ratio exceeds 5 at 1 bar the H_2/CO is higher than expected from the equilibrium conditions, this apparent higher value is because the CH_4 conversion at those conditions is lower than the predicted one at the chemical, therefore at low CH_4 conversion the H_2/CO ratio are non-linearly linked, so small changes in the conversion can make large changes in the H_2/CO ratio.

3.4. Reverse water gas shift reactor

The temperatures, pressures and feed gasses used to test the material's capabilities as RWGS catalyst are detailed in Table 4.

The temperature profile and outlet gas composition during RWGS at 1 bar_a, 10 NLPM and 900 °C are shown in Fig. 17. During the RWGS experiments, the furnace set point was kept constant to overcome heat losses to the environment. However, this continual heat addition dwarfed the loss in temperature due to the RWGS. After 12 min, the

Table 4
RWGS experimental conditions.

Reactor set point (°C)	Flowrate (NLPM)	Pressure (bar_a)	Gas composition (molar %) in balance of He
600	10	1 bar	10 % H_2; 30 % CO_2
		5 bar	10 % H_2; 40 % CO_2
			10 % H_2; 50 % CO_2
700	10	1 bar	10 % H_2; 30 % CO_2
		5 bar	10 % H_2; 40 % CO_2
			10 % H_2; 50 % CO_2
800	10	1 bar	10 % H_2; 30 % CO_2
		5 bar for CO_2 lean	10 % H_2; 40 % CO_2
			10 % H_2; 50 % CO_2
			20 % H_2; 10 % CO_2
850	10	1 and 5	20 % H_2; 10 % CO_2
900	10	1 bar	10 % H_2; 30 % CO_2
		5 bar for CO_2 lean	10 % H_2; 40 % CO_2
			10 % H_2; 50 % CO_2
			20 % H_2; 10 % CO_2

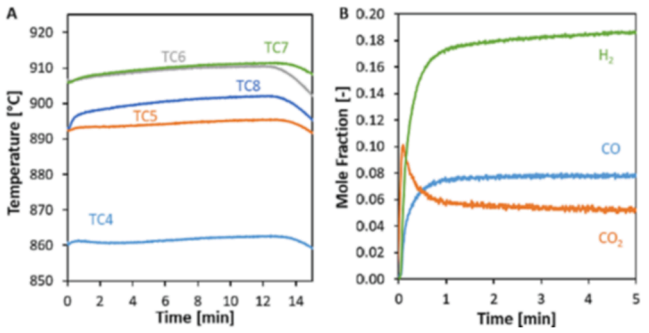

Fig. 17. Recorded temperature (A), outlet gas composition (B) during RWGS at 1 bar_a, 10 NLPM feed flowrate, 900 °C initial bed temperature and 10 % CO_2 and 20 % H_2 in the feed.

furnace power was switched off at which point the solid temperatures began to drop, but the extent that this is due to the heat losses to the environment and convective heat transfer along the reactor is not quantifiable. The outlet gas composition remained steady through the RWGS, achieving a H_2/CO above 2 throughout, as would be expected from a thermodynamically limited reactor [24]. This showed that the OC successfully operates as RWGS catalysts under these conditions confirming the suitability of the material to act as both OC and catalyst. In order to maintain a H_2/CO ratio of 2, even at 900 °C, some unconverted CO_2 will be present due to the thermodynamic limitation associated with RWGS. This is a common problem for Gas-to-liquid applications which is usually addressed by considering a CO_2 removal step in large-scale FT plants to reduce the equipment volume. Instead, for small-medium scale FT plant [38], high CO_2 content in the FT reactor is accepted as CO_2 behaves as inert/coolant gas in case of LT-FT Co-based catalyst for aviation fuels or participate to the reactions in view of active WGS in case of HT-FT with Fe-based catalyst.

Comparing the H_2/CO ratio for different temperatures and feed compositions (Fig. 18) it can be seen that low temperatures are not relevant for the process. In case of H_2/CO_2 ratio is equal to 2 (feed condition), at T > 800 °C the change in the composition is marginal. However, a higher H_2/CO_2 ratio (equal to 3 to 5) could reduce the final H_2/CO ratio to as low as 0.25 indicating that the syngas composition can be tuned by changing the feed conditions and controlled by the operating temperature.

At higher pressure (5 bar_a) the H_2/CO ratio of the products increases (but still within the 95 % uncertainty window) as shown in Fig. 19. The carbon and oxygen balance on the reactor (shown in the SI Figs. 2-S and 3-S) are also within uncertainty confirming that pressure does not have a consistently measurable effect on the reactor.

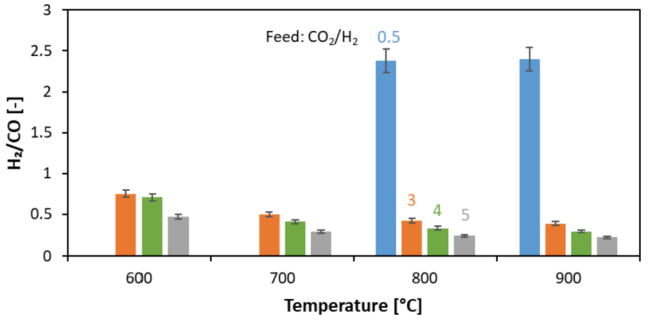

Fig. 18. H_2/CO ratio at the outlet as a function of temperature and CO_2/H_2 ratio at the inlet of the reactor at a total flowrate of 10 NLPM and 1 bar_a. With error bars of 1 standard deviation in the measured values.

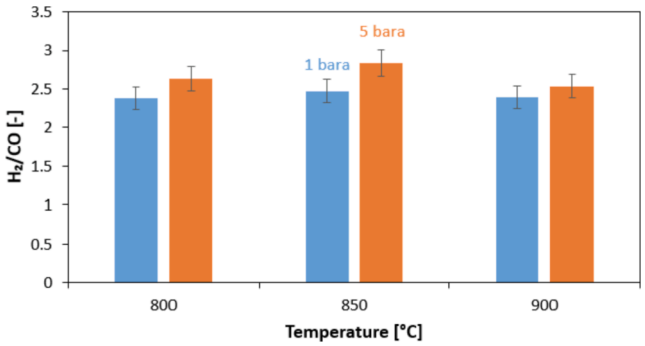

Fig. 19. CO/H_2 ratio at the outlet as a function of temperature and pressure at a total flowrate of 10 NLPM with a CO_2/H_2 of 0.5 at the inlet of the reactor. With error bars of 1 standard deviation in the measured values.

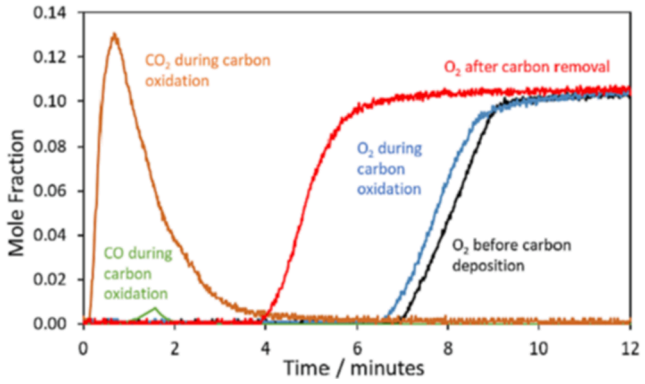

Fig. 20. Outlet gas analysis for oxidation at 700 °C and 1 bar using a mole fraction of 0.105 O_2, before carbon deposition, during carbon oxidation and after carbon removal.

3.5. *Effect of carbon deposition*

In order to test the resilience of the material to carbon deposition and over reduction the reactor was fed a stream of pure CO, fully reducing the OC to Fe at 900 °C. The flow of CO was then continued allowing carbon deposition. A series of different methods were used to revitalise the material. First, oxidation was carried out to remove any remaining carbon and returned the material to Fe_2O_3. The oxygen capacity of the bed had decreased by 41 % from 1.346 ± 0.002 mol of oxygen per kg of OC before carbon deposition to 0.828 ± 0.002 mol of oxygen per kg of OC when the carbon was removed (black vs orange line in Fig. 20). The

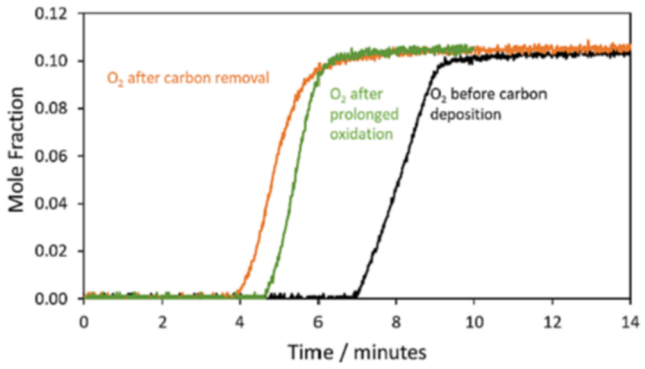

Fig. 21. Outlet gas analysis for oxidation at 700 °C and 1 bar using a mole fraction of 0.105 O_2, before carbon deposition, after carbon removal and after the reactor was held at 850 °C and 1 bar in an O_2 and CO_2 rich gas mixture for 4 h.

bed was removed to ensure that sintering had not occurred, but in the process, the repacked bed was situated 10 mm lower relative to the thermocouple and heated section of the bed.

The bed was then heated to 850 °C at 1 bar and held there for 4 h in a mixture of air and CO_2, this caused a slight increase in oxygen capacity varying the breakthrough time from 240 s to 276 s but failed to return the system to its original state. The outlet gas composition during the subsequent oxidation is shown in Fig. 21. This process increased the oxygen capacity to 0.928 ± 0.001 mol of oxygen per kg of OC. Repeating this did not further increase the oxygen capacity of the reactor beyond 69 % of the original capacity.

The material was then used as a reforming catalyst. Subsequent oxidations and reductions showed an increase in the O_2 capacity of the bed, returning to 1.168 ± 0.002 mol of oxygen per kg of OC after the first reforming, 1.224 ± 0.001 mol of oxygen per kg of OC after the second reforming and 1.242 ± 0.002 mol of oxygen per kg of OC after the third reforming returning the bed to 92 % of its original capacity. It is expected that this is due to the presence of H_2O present in the bed during the reforming process achieved the revitalisation of the bed (Fig. 22).

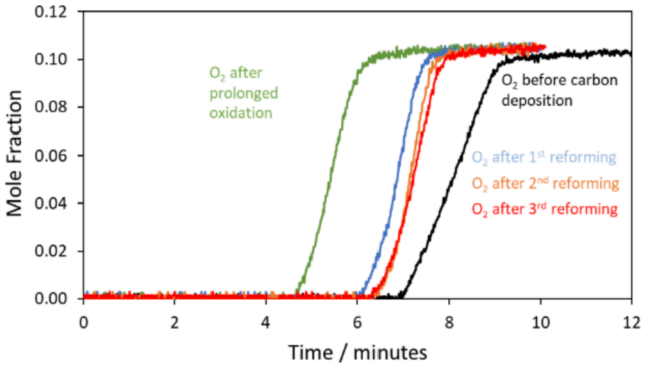

Fig. 22. Outlet gas analysis for oxidation at 700 °C and 1 bar using a mole fraction of 0.105 O_2, before carbon deposition, after the reactor was held at 850 °C and 1 bar in an O_2 and CO_2 rich gas mixture for 4 h and after a series of 15-minute methane reforming matching the conditions from Fig. 14.

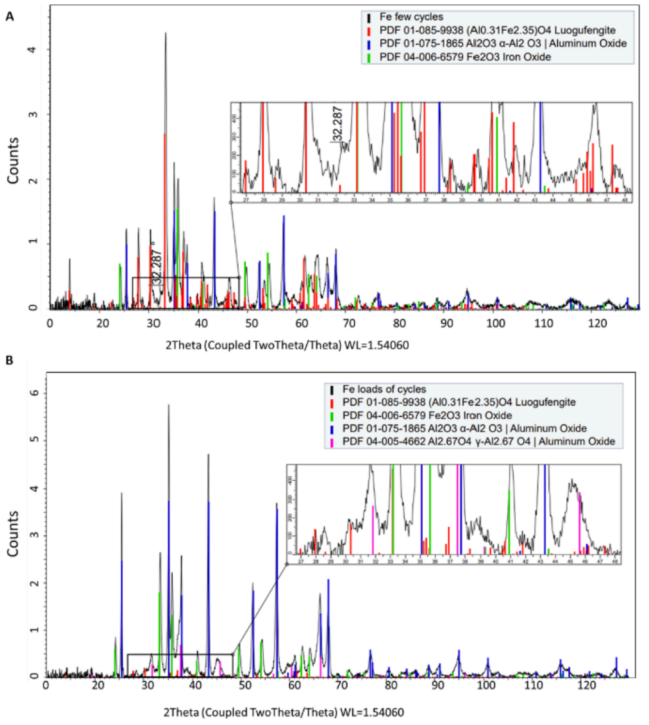

Fig. 23. Diffraction patterns from a pre carbon deposition (A) and post regeneration (B) sample with databased (PDF-4 + 2021) literature reflection positions from PDF01-085–9938, PDF04-006–6579, PDF 01–075-1865 and PDF 04–005-5662.

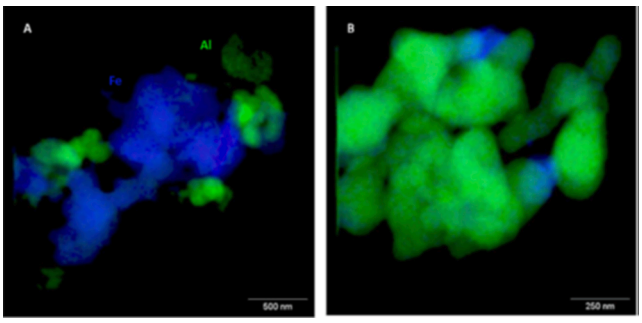

Fig. 24. TEM images of the OC before carbon deposition (A) and after regeneration (B) with Fe coloured blue and Al coloured green. (For interpretation of the references to colour in this figure legend, the reader is referred to the web version of this article.)

To determine what caused the drop in oxygen capacity, the material from the bed before carbon deposition and after the attempts to regenerate, the material was analysed using powder X-ray diffraction (XRD). Both materials were oxidised in air at 1 bar_a and 600 °C before being removed from the reactor. The comparison between the materials can be seen in Fig. 23. The Rietveld XRD analysis showed a large reduction in the peaks associated with Fe-containing compounds. This means that either the Fe atoms are no longer present or have lost their crystalline structure becoming amorphous. The lack of a broad low angle peak in the post-carbon removal sample is indicative that there has not been an increase in the proportion of the material that is amorphous, in fact the sample showed a slight decrease. This is however a qualitative measurement but indicates that the Fe has left the support.

The samples were also tested using transmission electron microscopy (TEM). This allowed for the distribution of Fe and Al on the surface of the material to be recorded Fig. 24. It can be seen from the images that the surface of the OC has a much lower proportion of Fe after the carbon was removed, confirming the findings from the XRD. The reduction in Fe from the material is expected to be because the carbon deposition caused the Fe detachment from the Al_2O_3 support, so once the carbon was removed, the Fe atoms were carried by the gas flow leaving the reactor and decreasing the capacity of the bed.

4. Conclusions

In this work, the experimental testing of Fe-based OC in dynamically operated packed bed chemical looping reactors was carried out to explore their feasibility as a process coupled with renewable sources such as biogas or green H_2 for CCU applications to produce carbon–neutral liquid fuels.

The main results of this study on Fe-based OCs can be summarised as follow:

- During the reduction step, CO_2 is required in the feed to avoid carbon deposition and excessive reduction to metallic Fe.
- Reduction using CH_4 only achieves 15 % CH_4 conversion, making biogas an unsuitable reducing agent from both the viewpoint of heat management and for capturing the CO_2 produced during reduction.
- CH_4 reforming conversion in dry reforming was limited to 62.8 %. A further study will focus on steam reforming in presence of H_2O to compare the two reactions.
- During RWGS, the system successfully formed a syngas mixture suitable for FT and tuneable H_2/CO ratio by modifying the H_2/CO_2 ratio in the feed, thus providing a new platform for RWGS. As the reaction is also endothermic, it can be integrated with chemical looping and resulting thermally balanced. This makes the CLRWGS a

valid alternative to other promising processes currently proposed for CCU and H_2 utilisation for liquid fuels and carbon neutral products.
- After the material was exposed to high CO content to deliberately obtain carbon deposition inside the bed, 92 % of the oxygen capacity could be recovered using CH_4 and CO_2. XRD and TEM analyses showed that this reduced capacity was due to the removal of Fe from the OC, which has been lost from the support indicating that a different preparation method could result in a more resistant OC.

Declaration of Competing Interest

The authors declare that they have no known competing financial interests or personal relationships that could have appeared to influence the work reported in this paper.

Data availability

Data will be made available on request.

Acknowledgements

The authors acknowledge the EPSRC project (BREINSTORM – EP/S030654/1) and the Department of BEIS in the framework of the Low Carbon Hydrogen Supply 2: Stream 1 Phase 1 Competition (TRN 5044/04/2021) (RECYCLE, HYS2137) for providing funding and support to the development of this study. We are grateful for the analysis support provided by the Johnson Matthey technology centre analytical team for the XRD, XPS, and TEM data collection. The authors would like to take this opportunity to recognize the important contribution to this paper, and many other areas of hydrogen and reforming technologies, of their late and much missed friend and colleague David Wails.

Appendix A. Supplementary data

Supplementary data to this article can be found online at https://doi.org/10.1016/j.cej.2022.139791.

References

[1] N.Z. Muradov, T.N. Veziroğlu, From hydrocarbon to hydrogen-carbon to hydrogen economy, Int. J. Hydrogen Energy 30 (2005) 225–237, https://doi.org/10.1016/j.ijhydene.2004.03.033.
[2] IEA, Technology Roadmap: Energy and GHG Reductions in the Chemical Industry via Catalytic Processes, 2015.
[3] A.M.W.P. Haussinger, R. Lohmuller, 2. Production Wiley (Ed.), Ullman's Encyclopedia of Industrial Chemistry (2012), pp. 249–298, in: Hydrogen, 2012.
[4] G. Collodi, G. Azzaro, N. Ferrari, S. Santos, Techno-economic Evaluation of Deploying CCS in SMR Based Merchant H2 Production with NG as Feedstock and Fuel, in, Energy Procedia, Elsevier Ltd (2017) 2690–2712, https://doi.org/10.1016/j.egypro.2017.03.1533.
[5] J.C. Abanades, B. Arias, A. Lyngfelt, T. Mattisson, D.E. Wiley, H. Li, M.T. Ho, E. Mangano, S. Brandani, Emerging CO2 capture systems, Int. J. Greenh. Gas Control. 40 (2015) 126–166.
[6] V.D.B.C. Dasireddy, D. Vengust, B. Likozar, J. Kovač, A. Mrzel, Production of syngas by CO2 reduction through Reverse Water-Gas Shift (RWGS) over catalytically-active molybdenum-based carbide, nitride and composite nanowires, Renew. Energy 176 (2021) 251–261, https://doi.org/10.1016/j.renene.2021.05.051.
[7] M. Rieks, R. Bellinghausen, N. Kockmann, L. Mleczko, Experimental study of methane dry reforming in an electrically heated reactor, Int. J. Hydrogen Energy 40 (2015) 15940–15951, https://doi.org/10.1016/J.IJHYDENE.2015.09.113.
[8] C. de Leeuwe, W. Hu, J. Evans, M. von Stosch, I.S. Metcalfe, Production of high purity H2 through chemical-looping water–gas shift at reforming temperatures – The importance of non-stoichiometric oxygen carriers, Chem. Eng. J. 423 (2021), 130174, https://doi.org/10.1016/J.CEJ.2021.130174.
[9] K.J. Lim, V. Spallina, Techno-Economic Assessment of Glycerol to Liquid Fuels Production using Chemical Looping Process, 2021.
[10] S.J. Gasior, A.J. Forney, J.H. Field, D. Bienstock, H.E. Benson, Production of synthesis gas and hydrogen by the steam-iron process: pilot-plant study of fluidized and free-falling beds, Bureau of Mines (1961).
[11] J. Adanez, A. Abad, F. Garcia-Labiano, P. Gayan, L.F. De Diego, Progress in chemical-looping combustion and reforming technologies, Prog. Energy Combust. Sci. 38 (2012) 215–282, https://doi.org/10.1016/j.pecs.2011.09.001.
[12] M. Luo, Y. Yi, S. Wang, Z. Wang, M. Du, J. Pan, Q. Wang, Review of hydrogen production using chemical-looping technology, Renew. Sustain. Energy Rev. 81 (2018) 3186–3214.
[13] D. Li, R. Xu, X. Li, Z. Li, X. Zhu, K. Li, Chemical looping conversion of gaseous and liquid fuels for chemicals production: A Review, Energy Fuels (2020), https://doi.org/10.1021/acs.energyfuels.0c01006.
[14] V. Spallina, B. Marinello, F. Gallucci, M.C. Romano, M. Van Sint Annaland, Chemical looping reforming in packed-bed reactors: Modelling, experimental validation and large-scale reactor design, Fuel Process. Technol. 156 (2017) 156–170, https://doi.org/10.1016/j.fuproc.2016.10.014.
[15] R.F. Kooiman, H.P. Hamers, F. Gallucci, M. van Sint Annaland, Van Sint Annaland, Experimental demonstration of two-stage packed bed chemical-looping combustion using syngas with CuO/Al2O3 and NiO/CaAl2O4 as oxygen carriers, Ind. Eng. Chem. Res. 54 (7) (2015) 2001–2011.
[16] V. Spallina, H.P. Hamers, F. Gallucci, M.S. Annaland, Chemical Looping Combustion for Power Production, Process Intensif, Sustain. Energy Convers. (2015) 117–174, https://doi.org/10.1002/9781118449394.CH5.
[17] K.M. Allen, A.M. Mehdizadeh, J.F. Klausner, E.N. Coker, Study of a magnetically stabilized porous structure for thermochemical water splitting via TGA, High-temperature-XRD, and SEM analyses, Ind. Eng. Chem. Res. 52 (2013) 3683–3692, https://doi.org/10.1021/ie302691e.
[18] M. Zhu, I.E. Wachs, Iron-Based Catalysts for the High-Temperature Water-Gas Shift (HT-WGS) Reaction: A Review, ACS Catal. 6 (2015) 722–732, https://doi.org/10.1021/ACSCATAL.5B02594.
[19] F. Bustamante, R.M. Enick, A.V. Cugini, R.P. Killmeyer, B.H. Howard, K. S. Rothenberger, M.V. Ciocco, B.D. Morreale, S. Chattopadhyay, S. Shi, High-temperature kinetics of the homogeneous reverse water–gas shift reaction, AIChE J. 50 (2004) 1028–1041, https://doi.org/10.1002/AIC.10099.
[20] C. Panaritis, J. Zgheib, S.A.H. Ebrahim, M. Couillard, E.A. Baranova, Electrochemical in-situ activation of Fe-oxide nanowires for the reverse water gas shift reaction, Appl. Catal. B Environ. 269 (2020), 118826, https://doi.org/10.1016/J.APCATB.2020.118826.
[21] J.A. Loiland, M.J. Wulfers, N.S. Marinkovic, R.F. Lobo, Fe/γ-Al 2 O 3 and Fe–K/γ-Al 2 O 3 as reverse water-gas shift catalysts, Catal, Sci. Technol. 6 (2016) 5267–5279, https://doi.org/10.1039/C5CY02111A.
[22] C. de Leeuwe, W. Hu, D. Neagu, E.I. Papaioannou, S. Pramana, B. Ray, J.S. O. Evans, I.S. Metcalfe, Revisiting the thermal and chemical expansion and stability of $La_{0.6}Sr_{0.4}FeO_{3-\delta}$, J. Solid State Chem. 293 (2021) 121838.
[23] E. Karimi, H.R. Forutan, M. Saidi, M.R. Rahimpour, A. Shariati, Experimental study of chemical-looping reforming in a fixed-bed reactor: Performance investigation of different oxygen carriers on Al2O 3 and TiO2 support, Energy Fuels 28 (2014) 2811–2820, https://doi.org/10.1021/EF5003765.
[24] D. Burgess, Thermochemical data, in: P. Linstrom, W. Mallard (Eds.), NIST Chem. WebBook, NIST Stand. Ref. Database Number 69, National Institute of Standards and Technology, Gaithersburg MD 20899, 2019. https://doi.org/10.18434/T4D303.
[25] P.A. Argyris, C. de Leeuwe, S.Z. Abbas, V. Spallina, Mono-dimensional and two-dimensional models for chemical looping reforming with packed bed reactors and validation under real process conditions, Sustain. Energy Fuels 6 (11) (2022) 2755–2770.
[26] P.A. Argyris, C. de Leeuwe, S.Z. Abbas, A. Amiero, S. Poultson, D. Wails, V. Spallina, Chemical Looping Reforming for syngas generation at real process conditions in packed bed reactors: an experimental demonstration, Submitt. to Chem. Eng. J. (2022).
[27] S. Chuang, J. Dennis, A. Hayhurst, S. Scott, Development and performance of Cu-based oxygen carriers for chemical-looping combustion, Combust. Flame 154 (1-2) (2008) 109–121.
[28] J.A. Medrano, H.P. Hamers, G. Williams, M. van Sint Annaland, F. Gallucci, NiO/CaAl2O4 as active oxygen carrier for low temperature chemical looping applications, Appl. Energy 158 (2015) 86–96, https://doi.org/10.1016/J.APENERGY.2015.08.078.
[29] S. Noorman, M. Van Sint Annaland, H. Kuipers, Packed bed reactor technology for chemical-looping combustion, Ind. Eng. Chem. Res. 46 (2007) 4212–4220, https://doi.org/10.1021/ie061178i.
[30] F. García-Labiano, J. Adánez, L.F. de Diego, P. Gayán, A. Abad, Effect of Pressure on the Behavior of Copper-, Iron-, and Nickel-Based Oxygen Carriers for Chemical-Looping Combustion, Energy Fuels 20 (2005) 26–33, https://doi.org/10.1021/EF050238E.
[31] C.L. Yaws, Yaws' Handbook of Properties of the Chemical Elements – Knovel, Knovel, 2011. https://app.knovel.com/web/toc.v/cid:kpYHPCE007/viewerType:toc/ (accessed July 9, 2020).
[32] M. Ortiz, F. Gallucci, T. Melchiori, V. Spallina, M. van Sint Annaland, Kinetics of the Reactions Prevailing during Packed-Bed Chemical Looping Combustion of Syngas using Ilmenite, Energy Technol. 4 (2016) 1137–1146, https://doi.org/10.1002/ENTE.201500511.
[33] A. Abad, J. Adánez, A. Cuadrat, F. García-Labiano, P. Gayán, L.F. de Diego, Kinetics of redox reactions of ilmenite for chemical-looping combustion, Chem. Eng. Sci. 66 (2011) 689–702, https://doi.org/10.1016/J.CES.2010.11.010.
[34] V. Spallina, F. Gallucci, M.C. Romano, M. Van Sint Annaland, Pre-combustion packed bed chemical looping (PCCL) technology for efficient H2-rich gas production processes, Chem. Eng. J. 294 (2016) 478–494, https://doi.org/10.1016/J.CEJ.2016.03.011.
[35] C.K. Cheng, S.Y. Foo, A.A. Adesina, Steam reforming of glycerol over Ni/Al2O3 catalyst, Catal. Today. 178 (2011) 25–33, https://doi.org/10.1016/j.cattod.2011.07.011.

[36] X. Cheng, Z. Gu, F. Li, X. Zhu, Y. Wei, M. Zheng, D. Tian, H. Wang, K. Li, Enhanced resistance to carbon deposition in chemical-looping combustion of methane: Synergistic effect of different oxygen carriers via sequence filling, Chem. Eng. J. 421 (2021), 129776, https://doi.org/10.1016/J.CEJ.2021.129776.
[37] B. Kamitakahara, No Title, NIST Cent. Neutron Res. Resour. (n.d.). https://www.ncnr.nist.gov/resources/ (accessed June 25, 2018).
[38] S. Pratschner, M. Hammerschmid, F.J. Müller, S. Müller, F. Winter, Simulation of a Pilot Scale Power-to-Liquid Plant Producing Synthetic Fuel and Wax by Combining Fischer–Tropsch Synthesis and SOEC, Energies 2022, Vol. 15, Page 4134. 15 (2022) 4134. https://doi.org/10.3390/EN15114134.